Origin of complex impact craters on native oxide coated silicon surfaces

Juha Samela* and Kai Nordlund
Department of Physics, University of Helsinki, P.O. Box 43, FI-00014 Espoo, Finland

Vladimir N. Popok
Department of Physics, Gothenburg University, 41296 Gothenburg, Sweden

Eleanor E. B. Campbell
Department of Physics, Gothenburg University, 41296 Gothenburg, Sweden
and School of Chemistry, Edinburgh University, West Mains Road, Edinburgh EH9 3JJ, Scotland
(Received 23 July 2007; revised manuscript received 9 November 2007; published 11 February 2008)

Crater structures induced by impact of keV-energy Ar_n^+ cluster ions on silicon surfaces are measured with atomic force microscopy. Complex crater structures consisting of a central hillock and outer rim are observed more often on targets covered with a native silicon oxide layer than on targets without the oxide layer. To explain the formation of these complex crater structures, classical molecular dynamics simulations of Ar cluster impacts on oxide coated silicon surfaces, as well as on bulk amorphous silica, amorphous Si, and crystalline Si substrates, are carried out. The diameter of the simulated hillock structures in the silicon oxide layer is in agreement with the experimental results, but the simulations cannot directly explain the height of hillocks and the outer rim structures when the oxide coated silicon substrate is free of defects. However, in simulations of 5 keV/atom Ar_{12} cluster impacts, transient displacements of the amorphous silicon or silicon oxide substrate surfaces are induced in an approximately 50 nm wide area surrounding the impact point. In silicon oxide, the transient displacements induce small topographical changes on the surface in the vicinity of the central hillock. The comparison of cluster stopping mechanisms in the various silicon oxide and silicon structures shows that the largest lateral momentum is induced in the silicon oxide layer during the impact; thus, the transient displacements on the surface are stronger than in the other substrates. This can be a reason for the higher frequency of occurrence of the complex craters on oxide coated silicon.

DOI: 10.1103/PhysRevB.77.075309 PACS number(s): 79.20.−m, 61.80.Jh, 83.10.Rs

I. INTRODUCTION

Atomic cluster beams are being explored for an increasing number of applications.[1] Understanding of the cluster collision dynamics that leads to the variety of observed structures on cluster impact with a substrate is needed to develop the applications further and to find new ways to process surfaces. Among the most important materials processed by cluster beams is silicon. A silicon wafer has a thin layer of native (natural) silicon oxide on its surface if it has been exposed to air under ambient conditions. Alternatively, the oxide layer can be intentionally grown using thermal oxidation or deposition techniques. Regardless of its origin, the oxide layer affects the results of ion or cluster beam processing, for example, the resulting dopant profile is different depending on whether the oxide layer is present or not.[2] Therefore, the application of cluster beams for surface smoothing, doping, and etching of silicon requires knowledge of the dynamics of cluster impact when the native oxide layer is present.

The aim of this work is to understand the formation of surface craters induced by cluster impact through the native oxide layer on a silicon wafer. There is experimental evidence for the existence of both complex crater structures consisting of a central hillock with a surrounding rim and just simple hillocks.[3–7] On the other hand, there are a number of experimental results showing the formation of simple craters on the impact of large (hundreds or thousands of atoms) clusters.[8–10] Formation of the simple craters in pure crystalline silicon is also very well simulated using molecular dynamics.[8,11,12] However, one should note that the diameters of the complex structures are considerably larger than the typical simple crater diameters and cannot be explained by referring only to the cratering (excavation) mechanisms.

The above-mentioned agreement between the experimental and the simulated results indicates that the simulation models are good approximations for the real cluster collision dynamics in many cases.[10,12,13] However, it might be necessary to include in the simulations an oxide layer for certain cluster-surface impact conditions in order to understand its effect on the formation of the complex craters and hillocks. The interatomic potential model should be able to describe reasonably well both *c*-Si, *a*-Si, *a*-SiO_2, and the interface between silicon and silica. In this work, we apply a silica model which is based on the well known Stillinger-Weber interatomic potential[14,15] for silicon and can be used to simulate the various silicon and silica structures.

The rest of this paper is organized as follows. The experimental methods are briefly reviewed in Sec. II, and the simulation methods are described in Sec. III. Both experimental and simulated results are discussed in Sec. IV. In Sec. V, we show that the displacement of the silica layer observed in the simulations is the most probable reason for the experimentally observed complex crater formation.

II. EXPERIMENTAL METHODS

The experimental setup is described in detail in Refs. 15 and 16. Here, we summarize only the features that are rel-

evant from the point of view of the results presented in this paper.

Argon cluster ion implantation with keV energies was carried out for nonsputtered (with the oxide layer) and sputtered (without the oxide layer) Si(111) in ultrahigh vacuum of $(1-2)\times 10^{-9}$ Torr. The native oxide layer thickness was found to be 2–3 nm using transmission electron microscopy. A commercial Ar^+ ion gun AG5000 (Vacuum Generators) with an ion energy of 1 keV was used for *in situ* sputtering of the target. The sputtering time was 10 min, providing the sputtering of approximately 10 nm thick layer, i.e., complete removal of the native oxide layer. After cluster implantation, the samples were first moved to lower vacuum of 10^{-7} Torr for about 30 min, where the oxidation can start, and then to the ambient atmosphere for the measurement. The surfaces were analyzed by a scanning probe microscope Ntegra (NT-MDT) in atomic force microscopy (AFM) tapping mode. Silicon cantilevers with ultrasharp diamondlike carbon tips (curvature radius of 1–3 nm) were used. Exposure of the implanted samples to low vacuum and especially to the ambient atmosphere prior to the AFM measurements leads to the renewal of a native oxide layer on the surface. This effect can be considerable, because the total exposure time varied from 40 min to a few hours for some samples. The oxidation is further discussed in Sec. V where we compare the simulations to the AFM results.

III. COMPUTER SIMULATIONS

The simulations were carried out using classical molecular dynamics (MD). The simulation arrangements and their suitability for cluster and ion bombardment simulations are discussed in Refs. 17–20. Here, we summarize the features which are essential from the point of view of this study.

The interaction model used in the simulations is described in Ref. 21. The model is based on the Stillinger-Weber potential for silicon.[14] We chose this model because it provides reasonable descriptions for both amorphous silica and silicon. Another reason was that the model is designed to reproduce the structure of compressively strained silica, which is an important property in the present study. In addition to the silica potential, a short-range repulsive potential[22] was smoothly joined to the silica and silicon potentials to prevent high-energy atoms moving too close to each other. Electronic stopping was applied as a nonlocal frictional force to all atoms having a kinetic energy larger than 10 eV.[22–24] The Stillinger-Weber potential[14,15] was used in the simulations where no silica layer was present.

The bulk silica structure used for the nonlayered a-SiO_2 target was built by copying a $3\times 3\times 3$ nm^3 cube that was first optimized with the Wooten-Winer-Weaire (WWW) algorithm[25,26] using a Keating potential[25,27] to have an ideal amorphous structure, and then relaxed with the silica potential used in the actual simulations.[21] The layered SiO_2/Si(111) structures were produced by combining an amorphous SiO_2 film and a Si(111) bulk structure and then letting the combined structure relax at the ambient temperature (300 K). The amorphous silica film was created from a quartz crystal by first melting it and then annealing it from

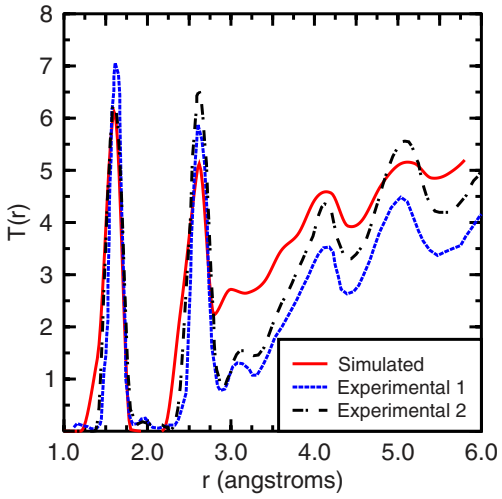

FIG. 1. (Color online) Comparison of the simulated radial distribution function (Ref. 33) $T(r)$ for a-SiO_2 to two experimental functions. The first experimental data are from Ref. 34 and the second from Refs. 26, 33, and 35.

4500 to 300 K in three phases. The combined structure was then relaxed at 300 K that was the ambient temperature in the simulations. This method produces a randomly ordered amorphous silica layer that forms a sharp interface with the supporting Si crystal. The WWW method was not used to create the oxide layer because of the risk of appearance of artificial topographical features in the silica film, if it was built of several identical WWW-optimized blocks. In the layered structures, the thickness of the silica layer was 2 nm, which is approximately the same as the thickness of the native oxide layer in the experiments.

Both the annealed and the WWW-optimized silica structures consist of SiO_4 tetrahedra where the Si–O bond length and O-Si-O angle distributions agree well with the experimental distributions. The average Si–O bond length in bulk amorphous silica is 1.615 Å, the average O-Si-O angle is 109.2°, and the average Si-O-Si angle is 141.8°. The corresponding experimental values for vitreous silica are 1.617 Å, 108.6°, and 145 ± 25°, respectively.[28] However, the mutual orientation of the tetrahedra varies more than in real amorphous silica, which is seen in Fig. 1 as a disagreement between the experimental and simulated pair correlations between 3 and 4 Å. The reason is the steric hindrance caused by the three-body term of the potential function, which is impossible to avoid completely by adjusting the parameters of the potential.[21] The density of the WWW-optimized amorphous silica was 2.1 g/cm^3, which is lower than the experimental value for vitreous silica of 2.2 g/cm^3.[28]

An environment dependent coefficient that is based on Hartree-Fock calculations is used in the potential to weaken the Si–O bonding depending on the oxidation number of Si atoms. We found that the model becomes unstable when the coefficient is calculated as described in Ref. 21. Therefore, the calculation is simplified in the present simulations. The changes are described in the Appendix. According to our tests, the changes do not considerably affect the structure of the silica-silicon interface or collision cascade development.

However, the environment dependence of the Si–O bond could be modeled in a better way in future versions of the potential.

In this study, we use the $SiO_2/Si(111)$ interface in order to be able to compare the results to the experimental observations. The silica potential describes the $SiO_2/Si(001)$ and $SiO_2/Si(111)$ interface in a way that is consistent with many experimental results.[21,29,30] It reproduces correctly x-ray diffraction peaks observed from thermally grown oxide films.[29,30] Although the $SiO_2/Si(111)$ interface is not created in the same way as in Refs. 29 and 30, the interface structures are quite similar. The surface energy for the simulated a-SiO_2 surface is 0.104 ± 0.004 eV/Å^2, and the corresponding experimental value is 0.064 eV/Å^2 or higher.[31] Therefore, we conclude that both the $SiO_2/Si(111)$ interface and the a-SiO_2 are reasonably well modeled for the purposes of this study. The surface energy for the simulated a-SiO_2 surface is 0.104 ± 0.004 eV/Å^2, and the corresponding experimental value is 0.064 eV/Å^2 or higher.[31] Therefore, we conclude that both the $SiO_2/Si(111)$ interface and the a-SiO_2 are reasonably well modeled for the purposes of this study.

In the simulations, the silica-silicon structures were bombarded with 1–120 keV Ar_{12} and Ar_{43} clusters. The incident angle was 0° in all cases. The impact point on the surface, as well as the spatial orientation of the cluster, was varied randomly between the simulation runs. The Ar clusters were created using a Lennard-Jones potential, but only the repulsive potential[22] was used in the Ar-Ar interactions in the bombardment simulations. In spite of the lack of attraction between the cluster atoms, the prepared clusters completely maintained their spatial configurations before they arrived for the surface, because the repulsive potential mainly acts within short ranges. The diameters of spherical Ar_{12} and Ar_{43} clusters were 0.7 and 1.3 nm, respectively.

Four kinds of cluster bombardment simulation were carried out. Energy deposition during the first 200 fs after impact was studied in the first type of simulations. In these runs, the sizes of the simulation boxes were around $10 \times 10 \times 10$ nm^3, which is large enough to contain the first phases of the cascade formation. Four different target structures were analyzed: c-Si covered with an a-SiO_2 layer, a-SiO_2, a-Si, and c-Si. In the second type of simulations, the central hillock formation at low cluster energies for the a-SiO_2/a-Si target was simulated for 20 ps using $19 \times 20 \times 21$ and $30 \times 32 \times 21$ nm^3 boxes, depending on the cluster energy. In the third type of simulations, the rim formation was studied in the a-SiO_2/a-Si target, when the box size was $61 \times 62 \times 31$ nm^3 containing 5.9×10^6 atoms. The simulations were followed up to 20 ps. Longer test runs with or without annealing showed that no structural changes that could affect the results occurred after 20 ps. Each of these large-scale simulations required 5000–6000 CPU hours, which limited the number of simulations to one run at each impact energy. In addition, test runs with even larger simulation cell ($100 \times 100 \times 43$ nm^3, 23 million atoms) verified that the boundaries of the smaller simulation boxes ($61 \times 62 \times 31$ nm^3) introduced no artificial surface topography changes. Rim formation on a-Si targets was studied in the fourth series of simulations where the target was a $39 \times 39 \times 32$ nm^3 amorphous silicon structure containing 2.5×10^6 atoms.

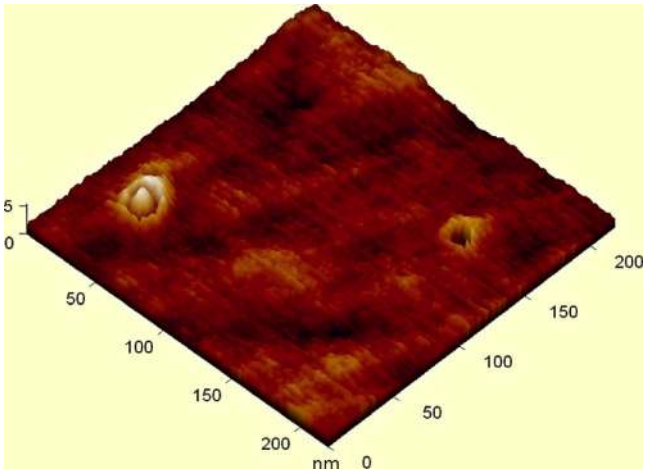

FIG. 2. (Color online) AFM image of a Si(111) surface with native oxide layer after the implantation of 12 keV Ar_{12}^+ cluster ions. A complex (left) and a simple crater (right) are shown.

The sizes of rectangular simulation boxes were chosen to be large enough to include whole collision cascades and to prevent boundary effects from distorting the cascades. Shock waves can affect the results, if they bounce back from the boundaries of the simulation cell or come back through the periodic boundaries. The techniques used in this work are described in Ref. 17. In addition to the normal shock waves induced by the impacts, the displacements in the silica layer reach an area whose diameter is more than 20 nm. The simulation cell used in the large-scale runs becomes too small, and artificial boundary effects appear when the Ar_{12} cluster energy is more than 60 keV/cluster. Therefore, the analysis of outer rims is done at 60 keV/cluster or lower energies.

There is evidence that the real oxide layers have slightly different structures depending on the mechanism that created the layer. For example, some thermal oxide layers are not randomly oriented but reflect the crystal orientation of the supporting crystal, whereas deposited oxides have a different structure.[32] In general, the order in the target affects channeling probabilities and direction of the cluster atoms, but small variations in the structure of the silica-silicon interface are not likely to change the overall mechanisms of cluster stopping. The Si(111) surface is chosen as the supporting structure since it is used in the experiments. The probability of cluster atom channeling is smaller in Si(111) than in Si(100) under the normal angle of incidence; thus, the results in the a-$SiO_2/Si(100)$ structure may be different than obtained in this study for the a-$SiO_2/Si(111)$ system.

IV. RESULTS

A. Experimental observation of craters and hillocks

In earlier experiments on Ar_n^+ cluster ion implantation (n from 11 to 55) with energies of 3–18 keV/cluster into Si(111) covered with a native oxide layer, the formation of simple craters, hillocks, and complex craters (craters containing a centrally positioned hillock) was found.[4,5] A typical

AFM image of the surface area with complex and simple craters is shown in Fig. 2. The hillock heights were found to decrease from 2.5 to 0.5 nm with an increase in the implantation energy from 3 to 18 keV/cluster, and the basal hillock diameters do not depend on the energy varying between 10 and 20 nm.[5] Although the height precision of the AFM measurements is typically $\leqslant$0.2 nm, the lateral dimensions are imaged with distortion due to the finite curvature of the tip. The rim-to-rim diameter of the simple craters was found to be 10–15 nm, whereas the rim-to-rim diameters of the complex craters were found to be larger, 30–50 nm.[5]

In the current experiments, the implantation of 3 keV $Ar^+_{16\pm3}$ cluster ions into nonsputtered silicon leads to the formation of similar surface defects as those found earlier on the implantation of 3 keV Ar^+_{12} and Ar^+_{22} cluster ions, i.e., predominantly complex craters and hillocks with the heights of 2–3 nm. However, when the sample was sputtered and then implanted by Ar clusters under the same conditions, neither craters nor hillocks were found using AFM. One of the possible reasons is radiation damage of a thin surface layer of Si by the high-fluence Ar^+ ion beam used for the sputtering. According to SRIM-2003 (Ref. 24) simulations, the thickness of the damaged layer can be 2–3 nm, which is comparable with the simulated projected ranges of the cluster constituents. We expect that the layer is highly damaged containing vacancy complexes.[36] Therefore, the energy dissipation mechanism can be rather different from the mechanism in amorphous but compact material, and the AFM results are not comparable to simulated results in this case.

To eliminate the effect of radiation damage originated by the sputtering, the samples for the next series of cluster implantations were annealed *in situ* after sputtering at a temperature of 550 °C for 15 min. The annealing was done by resistive heating of the sample carrier. This annealing should lead to the recrystallization of the damaged layer.[37] Both nonsputtered and sputtered plus annealed samples were implanted by 15 keV $Ar^+_{43\pm3}$ cluster ions. On the nonsputtered samples, both complex and simple craters were found, similar to the case of 15 keV Ar^+_{54} cluster ion implantation reported earlier.[5] Additionally, plateaulike protrusions with basal diameters of around 50 nm and heights of 1.5–2.0 nm were observed. Some of the protrusions have a centrally positioned hillock increasing the total height up to 3 nm as shown in Fig. 3. However, on the sputtered and annealed sample, predominantly hillocks (without surrounding rim) with heights of 1.5–2.0 nm and basal diameters of 15–20 nm were observed (Fig. 4). The total ratio of the complex craters or plateaulike protrusions to simple hillocks is decreased to less than 10%. For the sample with the oxide layer, the complex structures are dominant, and their ratio is 60%–70% compared to simple hillocks. This result shows that the complex structures are more common when the native oxide layer is present.

B. Simulated craters and hillocks

In the simulations, the mechanism of crater formation in silica-silicon substrates is, in principle, similar to the mechanism found in simpler structures such as fcc metals. The mechanism is discussed in detail in Refs. 38 and 39; thus, we summarize it here only briefly. The energy deposited from the cluster atoms in collisions with the target atoms in the 2–4 nm surface layer melts the amorphous silica layer and, depending on the energy, the topmost layers of crystalline silicon. The rapid melting induces a pressure outward from the cluster track, and a cascade of displaced atoms expands laterally. Meanwhile, a crater is opened at the surface. The most energetic atoms sputter out of the crater, whereas atoms that have lower energies form the rim around the crater. At low cluster energies, the craters are narrow and their form is irregular. In some cases, no crater is visible but only a hillock appears on the surface. As the energy increases, craters become wider and deeper, which is typical in cluster impacts.[12,39] The height of the rim in the simulations also increases with cluster impact energy. The qualitative differences in crater formation between the different target materials are discussed in Ref. 40.

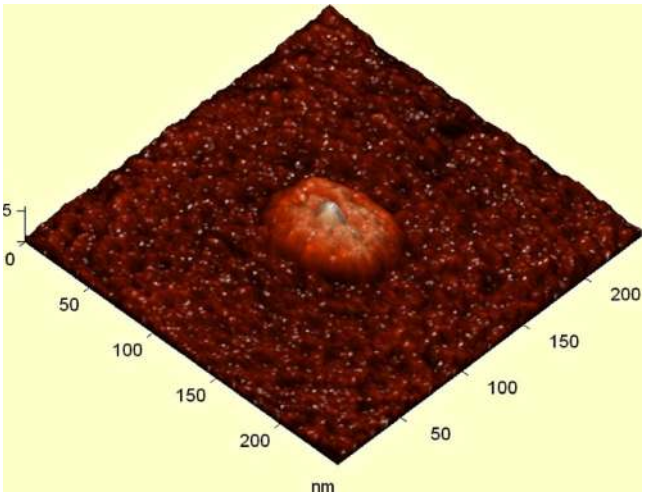

FIG. 3. (Color online) AFM image of a Si(111) surface with native oxide layer after the implantation of 15 keV Ar^+_{43} cluster ions. A plateaulike protrusion is shown.

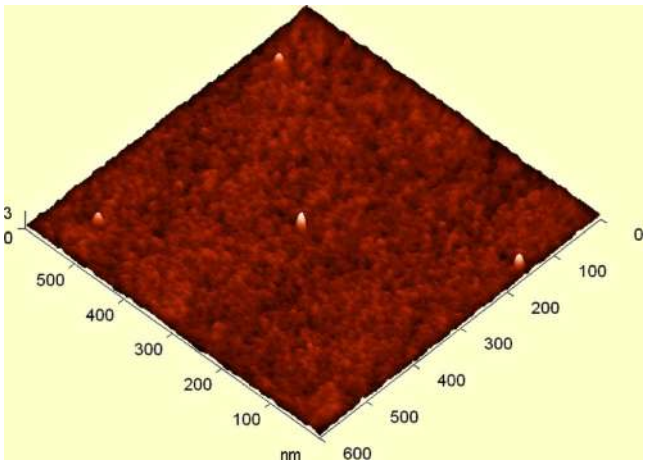

FIG. 4. (Color online) AFM image of sputtered Si(111) surface (i.e., no oxide layer) after the implantation of 15 keV Ar^+_{43} cluster ions. Predominantly hillocks are observed in this case.

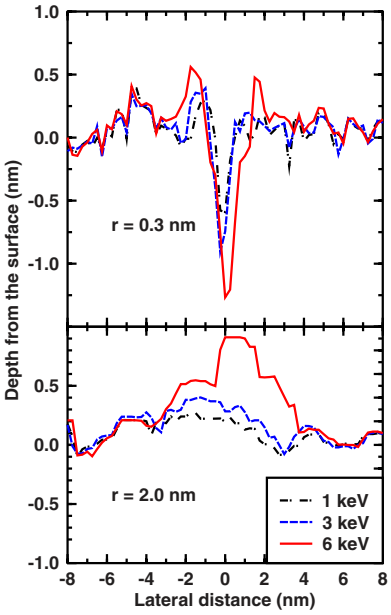

FIG. 5. (Color online) Average simulated surface profiles of the hillock region after Ar_{12} cluster impact on the silica-silicon structure (five runs at each energy). The upper frame shows the profile calculated emulating an ideal spherical AFM tip of radius of 0.3 nm. The lower frame is calculated from the same data but emulating a 2 nm radius tip. The height of the hillock in the bottom frame is higher than 0.5 nm, because the larger tip touches peaks on the surface that are not visible in the surface profile shown in the upper frame.

Figure 5 shows the average MD simulated surface profiles at different energies after 1–6 keV Ar_{12} impact on the silica-silicon substrate. The profiles are calculated using a procedure that emulates an AFM tip approaching the surface. In this procedure, the target surface is detected when the spherical surface of the tip that is approaching the target touches a target atom for the first time. The point where this occurs is not necessarily the lowest point of the spherical tip surface. Thus, the resulting profile depends on the radius of the tip. As can be seen in Fig. 5, the very sharp crater and rim shapes near the impact point appear as a hillock when the radius of the emulated tip corresponds to radius of a typical experimental AFM tip (tip convolution effect). Because the rim is not symmetric, the profile varies also depending on the direction of measurement across the crater. When calculated emulating a 2 nm tip, the apparent hillocks induced by Ar_{12} clusters are 5–10 nm wide and 0.3–1.0 nm high at energies of 1–15 keV/cluster. The width is rather consistent with the experimentally determined hillock diameters, considering the tip convolution effect. However, the experimentally measured hillocks are approximately three times higher than the hillocks seen in the simulations. A possible explanation for this discrepancy is discussed in Sec. V.

We conclude that the simulations can reproduce the simple crater forms observed in the silica-silicon targets. We can also suggest that some of the observed hillocks could represent the rims of narrow craters for which the crater opening could not be resolved by the AFM technique. However, the outer rim-to-rim diameters of the complex craters seen experimentally are found to be 30–50 nm at 1–18 keV/cluster.[5] Thus, their size is considerably larger than the diameter of the displacement cascades induced by cluster impact in the simulations, even when the cluster energy is 60 keV. Such large rim structures or plateaulike structures are not found in the simulations or our earlier studies of craters on fcc metals and on pure silicon structures.[38,39]

C. Cluster stopping and energy deposition

Three main phases of the energy deposition can be identified. In the first phase, which lasts no longer than 200 fs, the cluster atoms collide with the target atoms. The primary knock-on atoms may gain high kinetic energies and momenta. The cluster atoms transfer their energy also to the bonding electrons of the target, but this electronic stopping mechanism is weak compared to the atomic collisions at the energies simulated in the present study.[24] In the simulations, the electronic stopping decreases the kinetic energy of the moving atoms but is not further considered in the simulation model. In the second phase, the knock-on atoms transfer some of their energy to other target atoms and, if the energy is high enough, a continuous region of displaced atoms is formed. The displacement cascade is the main cause for the formation of craters and hillocks, as described in the previous section. The rim formation and sputtering lasts 5–10 ps. In the third phase, the system cools to ambient temperature and the structures change their form and may even disappear. After 20 ps, no further changes in morphology were seen in the simulations. In addition to these three phases of displacement cascade development, there is a post-impact phase when the structures are subject to oxidation due to exposure to ambient atmosphere. The morphology of the crater region may be influenced by this. The oxidation is not simulated in this work.

Figure 6 shows how the energy is transferred from Ar_{12} clusters to different targets at different cluster impact energies. The clusters that have energies equal or less than 6 keV deposit almost all their energy in the 2 nm thick surface layer regardless of the layer type. Thus, the vertical energy distribution immediately after the cluster has stopped is very similar regardless of the target type at these energies, and the resulting displacement cascades are located near the surfaces. The differences in cluster stopping become apparent only when the cluster energy is higher than 15 keV/cluster. The more energetic clusters penetrate deeper into the target, especially in *c*-Si, where the cluster atoms can channel through the substrate. Amorphous silica stops the high-energy clusters more effectively than amorphous silicon, although the O atoms present in silica stop the Ar atoms less than Si atoms in binary collisions due to their smaller mass and nuclear charge. Because the simulated cluster stopping is different between *a*-Si and *a*-SiO_2 only at the high energies, we believe that the difference is due to the mechanisms which the energetic cluster atoms coherently penetrate into the substrate.

The amorphous silica layer captures a significant portion of the cluster energy before the cluster atoms enter the *c*-Si. Thus, the silica layer protects the crystalline silicon wafer

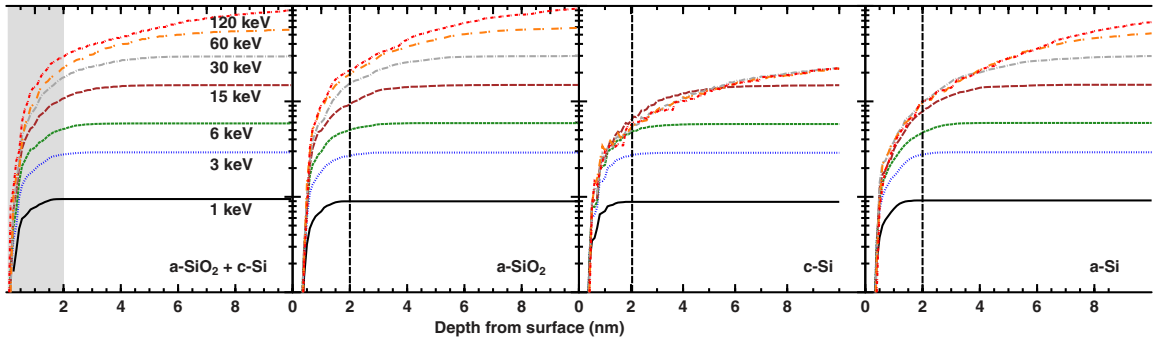

FIG. 6. (Color online) Energy deposited from Ar_{12} clusters calculated for different impact energies on different targets. The targets from left to right are crystalline (111) silicon covered with 2 nm silica layer, amorphous silica, crystalline silicon, and amorphous silicon. The gray area shows the location of the silica layer in the first target. The results are averages of nine simulations.

very effectively. However, the stopping effect of the a-SiO_2 is not so strong. (Note that the y axis is logarithmic in Fig. 6.) As discussed in Sec. III, the silica-silicon interface affects the structure of the oxide layer; thus, it has a slightly different atomic structure than the bulk oxide substrate. The two leftmost frames in Fig. 6 show that the a-SiO_2/c-Si system effectively stops the cluster more than the pure a-SiO_2 at energies higher than 6 keV/cluster. Although the cluster has to penetrate a 2 nm silica surface layer in both cases, the cluster loses more energy in this layer in the a-SiO_2/c-Si system than in the pure a-SiO_2 target. Because the difference is apparent only at the high energies, we conclude that it is related to the probability of strong head-on collisions between cluster and target atoms, similar to simulations of gold targets that show that the number of single strong collisions increases with the cluster energy.[39] Figure 7 shows that some atoms can travel considerably long distances between subsequent strong collisions also in the amorphous silica, although the mean free path of an atom in an amorphous substrate is much shorter than in crystals where channeling occurs. The strong collisions are more probable at the silica-silicon interface than in bulk amorphous silica. Although the interface is quite sharp, its effect reaches over some distance to the silica layer, and therefore the collision probability is already higher in the silica layer before the cluster atoms cross the interface.

In Fig. 7, some atoms are seen to depart from the main bundle already in the surface layer. This phenomenon is slightly stronger in the a-SiO_2/c-Si system, where more tracks are bent in the oxide layer than in the corresponding layer in the pure silica system. This confirms the conclusion that the silica layer stops some of the cluster atoms effectively. The strong collisions in the silica layer and at the silica-silicon interface change the direction of the cluster atoms, and a larger lateral momentum is induced in the target than in the pure silica substrate. In both cases, the cluster atoms prefer certain routes because the medium range structures of the amorphous substrates provide routes which are more open for atom movement than some alternative routes. At energies less than 15 keV, most of the cluster atoms stop in the surface layer regardless of the target type. At 120 keV, the cluster atoms have almost rectilinear trajectories through the silica layer.

The energy is transferred from the cluster atoms to the substrate during the first 200 fs after the collision. As a consequence, an expanding collision cascade is formed, where the primary knock-on atoms transfer their energy further to the secondary and tertiary knock-on atoms. The form of the cascade and its momentum distribution depends on the primary knock-on atom distribution determined by collision sequences of the cluster atoms as well as on the structure of the

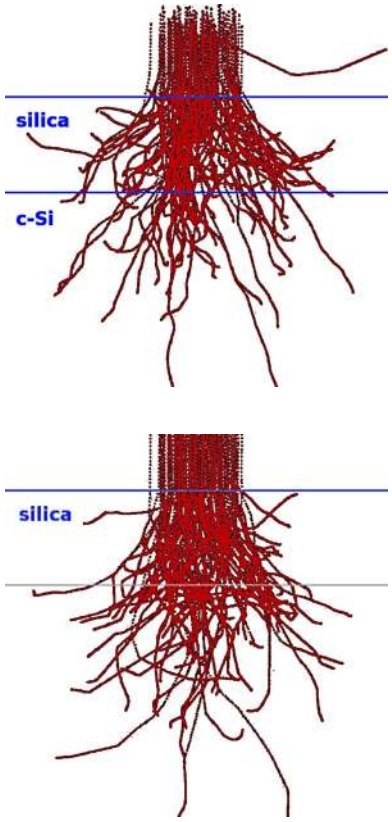

FIG. 7. (Color online) Tracks of 15 keV Ar_{12} cluster atoms during the first 200 fs. The results for the silica-silicon target are shown in the top frame and for the amorphous silica structure in the bottom frame. The tracks are collected from nine simulations, where the initial position and orientation of the cluster were varied randomly. The side length of the frames corresponds to 8 nm. The lower horizontal line in the top frame shows the position of the silica-silicon interface. The same depth level is marked in the bottom from for comparison, although no real interface is present.

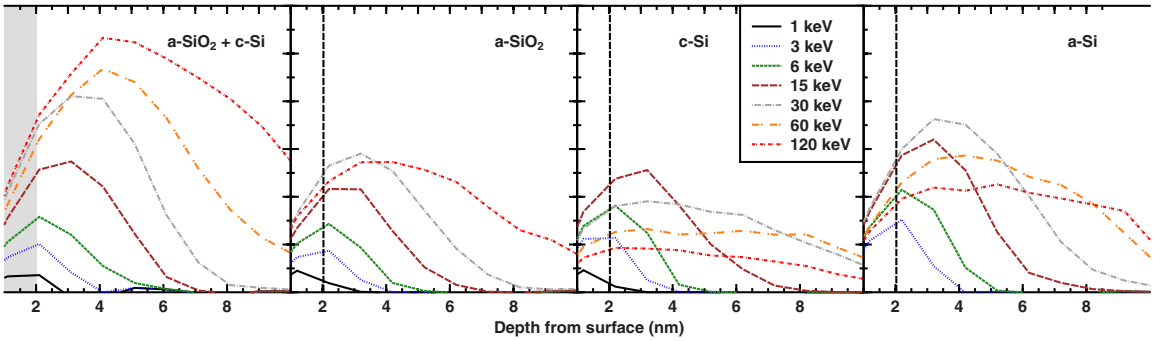

FIG. 8. (Color online) Comparison of the lateral momenta induced in the various substrates after the cluster atom stopping phase. The curves show the sum of lateral momenta of the target atoms around 200 fs after the impact of an Ar_{12} cluster as a function of depth. The lateral momentum of an atom is the component of its total momentum in the plane parallel to the surface and to the direction pointing outward from origo (positive values) or toward origo (negative values). Physically, the sum of atomic lateral momenta describes how strong the coherent outward movement of atoms in a particular layer is, in other words, how strong is the expansion of the collision cascade after the cluster atoms have deposited their energy.

target. The primary knock-on atoms are induced along the tracks of the cluster atoms; thus, the primary atom distribution is similar to the bundles shown in Fig. 7. However, the initial energies and momenta of the primary knock-on atoms vary along the tracks, and the collision cascade expands mainly in the directions where the largest total momentum is induced. The coherent movement of knock-on atoms also induces the displacement cascade, if the moving atoms are near enough to each other and their kinetic energy is high enough to destroy or melt the target structure. The final result of the displacement cascade is a crater; if the displaced atoms escape to vacuum, or a structurally changed region like the amorphous region typically surrounding the craters in *c*-Si. In the last phase of the collision cascade expansion, the outward momentum is not strong enough to destroy the substrate structure but only compresses the structure around the melted region and usually induces also an outward pressure wave. The response of the substrate to the compression and pressure wave outside the crater region is almost elastic, and the structure recovers after the compression. However, structural changes may occur depending on the substrate species. Amorphous silica consists of rigid SiO_4 tetrahedra that can move easily relative to each other easily. Therefore, the average silica structure may remain unchanged during the compression phase, although the mutual orientations and positions of the tetrahedra are changed.

Because in this study we are mostly interested in the possible structural changes outside the main crater region, and since the location of these changes presumably depends on the field of atomic momenta induced in the substrate, we calculated the lateral momentum distributions in the various substrates at 200 fs when the energy and momenta of the cluster atoms are transferred to the substrate and the collision cascade is starting to expand (Fig. 8). The structural changes induced by the expansion are more probable in the directions where the outward lateral momentum is large.

Figure 8 shows the differences between momenta induced in the substrates. The expansion of the collision cascade at 200 fs clearly depends on the substrate. The largest lateral momentum is induced in the a-SiO_2/c-Si system. Especially at energies higher than 15 keV/cluster, the lateral movement in silica-silicon interface is strong compared to the movement at the a-SiO_2 at the same depth. This is a consequence of strong collisions in the silica layer that stop the cluster atoms effectively and also bend trajectories of the cluster atoms toward lateral directions. Because of this bending, the cluster atoms enter the *c*-Si layer at various angles and the induced lateral momentum in the *c*-Si layer is larger than in the pure *c*-Si.

The second largest lateral momentum is induced in the *a*-Si substrate. Ar atoms are stopped in a-SiO_2 less effectively than in *a*-Si, because the oxygen atoms are lighter than silicon atoms, and less lateral momentum is deposited in the surface layers of a-SiO_2. However, at 120 keV/cluster, the lateral momentum in a-SiO_2 is larger, which indicates that the collision mechanisms are different at high energies. The analysis of this phenomenon is beyond the scope of this paper.

The effect of channeling is clearly shown in the case of *c*-Si (Fig. 8). At energies higher than 15 keV, the lateral velocity in the surface layers decreases with energy, indicating that the displacement cascade becomes narrower and deeper. A consequence is that the craters become smaller, and the sputtering yields decrease with increasing energy, as is shown in Refs. 38 and 39. A similar but weaker penetration effect is observed also in *a*-Si.[41] The reason for this is not channeling, but the clearing-the-way effect[42,43] due to the collective motion of the cluster atoms. In the a-SiO_2/c-Si system, neither the channeling nor clearing-the-way effect was seen. Instead, a strong lateral momentum is induced also in the *c*-Si layers beneath the silica layer. This momentum also forces the silica layer to move outward from the impact point, which is discussed in Sec. IV D.

Figure 9 shows that more energy is deposited in the silica layer when the cluster nuclearity (number of atoms) increases from $N=12$ to $N=32$ and the kinetic energy of the cluster E_{kin} is constant. In other words, the range of the cluster atoms is shorter. Because the momentum of a cluster atom is $p=\sqrt{2mE_{kin}/N}$, the momentum of the Ar_{32} atoms is less than the momentum of atoms of Ar_{12}. Thus, the result

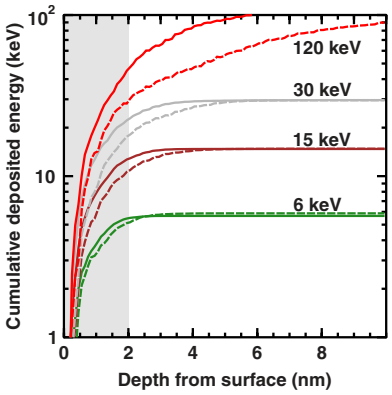

FIG. 9. (Color online) Comparison of cumulated deposited energy from the Ar_{32} (solid lines) and Ar_{12} (dashed lines) clusters at different impact energies as a function of depth. The gray area shows the location of the silica layer. The results are averaged over nine simulations.

shown in Fig. 9 indicates that the range of cluster atoms in the silica-silicon substrate depends on their momentum. This happens because the cluster atoms collide with the target atoms rather independently of others during the primary collision phase, although the atoms are quite near each other and the interatomic potential used in this work describes also three-body interactions in addition to the pair interactions. The same phenomenon is found in simulations of Ar cluster collisions on *a*-Si (Ref. 41) and in simulations of high-energy Au cluster collisions in Au.[39] It was also experimentally shown on Ag cluster implantation into graphite.[44]

D. Changes of surface morphology

In spite of the relatively large lateral momentum induced in the silica layer, no large and clear permanent modifications, such as outer rims or plateaulike structures, could be seen in the simulated surface profile of the *a*-SiO_2/*c*-Si system surrounding the primary crater rim. However, there is a transient displacement of surface atoms relative to their initial positions, which may induce changes in surface topography. Next, we discuss this displacement of atoms during the collision cascade development.

The course of events is seen in Fig. 10. The surface layer first moves outward from the impact point due to the lateral momentum induced in the substrate and then back until a stable state is reached around 20 ps. A small (<3 Å) average outward displacement occurs first and is followed by an average inward displacement. On the atomic level, the displacement field is, however, not uniform. The amorphous silica structure consists of quite rigid tetrahedra which can move relative to each other. This causes nonuniform radial displacements when the structure is pushed away from the impact point. Most of these changes of positions and heights are small, 1–5 Å. The formation of the circular displacement is seen in simulations of 100×100 nm^2 surfaces; therefore, it is very unlikely that the phenomenon would be a consequence of the boundaries of the simulation box. At lower energies, only very small displacements on the surface are found.

The *c*-Si layer, which responds elastically to the impact, moves first down and then bounces up due to the impact (Fig. 10). This vertical movement may strengthen the hillock formation and sputtering. In addition to vertical movement, the atoms are pushed away from the center because of the lateral momentum induced in the silica layer and also because momentum is induced in the *c*-Si atoms below the silica layer at high energies. The depth of the displacement cascade increases with increasing cluster energy, and at high energies, the cascade reaches the *c*-Si layer. As shown in Fig. 6, a larger proportion of the impact energy is deposited in the *c*-Si layer when the impact energy is high, and also the lateral momentum increases with the impact energy (Fig. 8). Therefore, we conclude that the lateral movement of the underlying *c*-Si atoms is the main reason for the displacement of the oxide layer.

The transient displacement of the surface layer occurs also in the *a*-SiO_2 and the *a*-Si targets (Fig. 11). In *a*-Si, the displacement is smaller than in the oxide coated system, the surface is finally displaced toward the crater, and peaks are not observed. In *a*-SiO_2, the displacement is similar to the displacement in the oxide coated system but smaller. In all cases, the displacement frontiers propagate approximately to 8 nm/ps. The displacements become larger when the cluster energy increases as shown in Fig. 12. In summary, the transient displacements are stronger and the modifications are more probable in the area surrounding the central crater or hillock if the oxide layer is present.

E. Oxide layer structure

The structure of the oxide layer plays an important role in the impact process. First, it stops the clusters, effectively protecting the *c*-Si substrate and bending the cluster atom trajectories so that the channeling in *c*-Si decreases. Second, peaks are induced on the oxide. Next, we discuss the oxide layer structure that leads to these two phenomena.

During the outward and inward movement of the silica layer, some peaks that are as high as the crater rim are formed on the surface because small regions of the silica layer move relative to each other. Figure 13 shows the top and side views of a 60 keV/cluster event. Emulating a 2 nm AFM tip, the peaks appear rather wide, but the forest of peaks is not dense enough to appear as a uniform plateau similar to that shown Fig. 4. Approximately ten times more peaks would be needed to form a plateaulike structure. Peaks appear systematically on oxide surfaces in all simulation runs, and the number of peaks increases with the cluster energy. The location of peaks seems to be random within the area where the displacement of the silica layer occurs. A full statistical analysis of the number and location of peaks at different energies is not possible in practice at the moment because of the huge amount of computing time it requires.

Figure 14 shows that the oxide layer consists of tetrahedral silica structures and the interface to the *c*-Si substrate is abrupt. Because the interface is relaxed in MD, it is not optimized to its lowest energy minimum. Compared to the optimized SiO_2/Si(001) interface,[45] more coordination defects can be seen. The interface induces strain in the Si layers

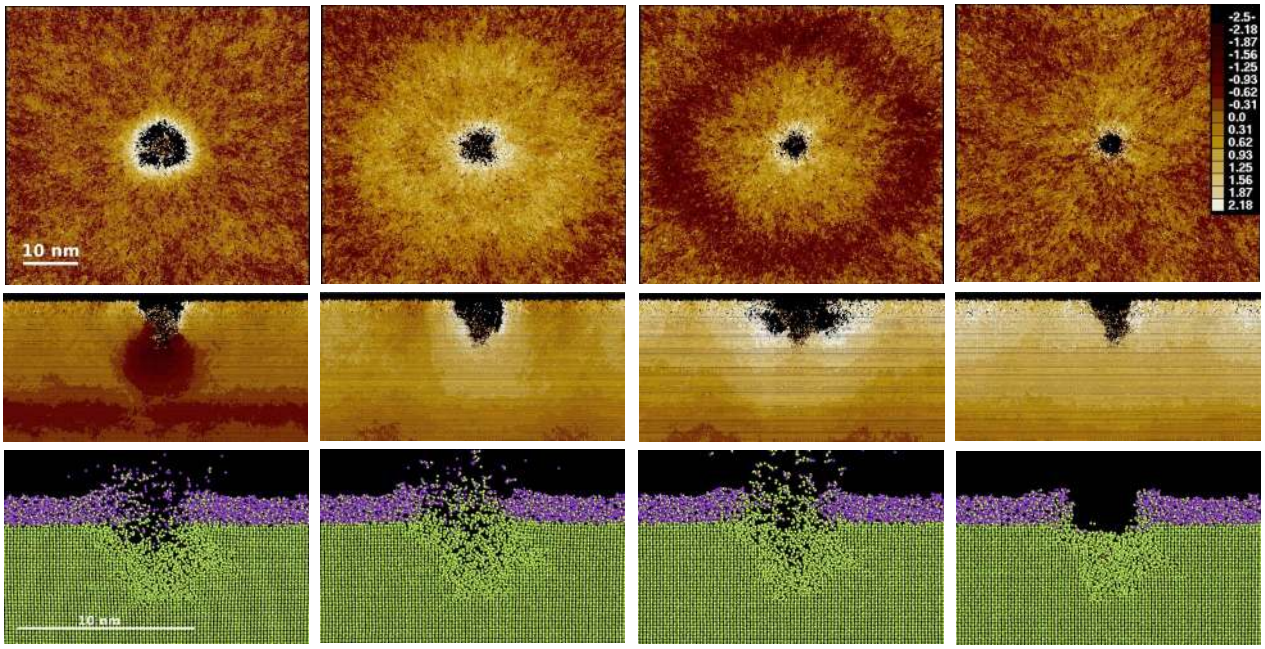

FIG. 10. (Color online) Visualization of a simulated 60 keV Ar_{12} cluster impact on the a-SiO_2/c-Si target. The snapshots from left to right are 1, 3, 5, and 20 ps after the impact. The upper row shows top views (60×60 nm^2) of the surface seen toward the impact zone. The colors illustrate the displacements of the atoms relative to their initial positions before the impact. The light colors in the top view indicate displacements outward from the origin (impact point) and the dark shades, displacements toward the origin. The middle row shows a side view, perpendicular to the surface. In this case, the light colors show upward displacements. The color scale ranges from −2.5 to 2.5 Å. The bottom row shows the position of atoms. Si atoms are green and O atoms blue in the online version.

below the interface and in the oxide layer (Fig. 15). The extra energy due to the strain and incomplete coordination is the difference ΔE between the potential energies of the interface structure and corresponding separate WWW-optimized a-SiO_2 and c-Si structures relaxed with the same interatomic potential. The largest contribution to this strain energy comes from the 2 nm thick layer around the abrupt interface. In this layer, the extra energy is 2.3 J/m^2. The total strain energy, including the contributions of the c-Si substrate and the whole oxide layer, is 4.4 J/m^2. Compared to the ideal amorphous silica, the number density is about the same in the middle of the oxide layer but lower near the interface. The O–Si bonds are 0.01 Å longer on average at the vicinity of the interface than near the surface. However, the number density of Si decreases gradually over the interface from its c-Si value to its value in bulk a-SiO_2. Thus, the Si content of the oxide layer is higher than in bulk a-SiO_2, which increases stopping power. The stress around the SiO_2/Si(111) interface is studied also in Ref. 46 using the same silica potential that is used in this study. In that work, it was found that the pressure induced by the interface is very small in the Si bulk but reaches over 2 nm to the silica side and is 10–17 GPa. This result is consistent with our findings. In conclusion, the higher stopping power compared to bulk a-SiO_2 that was discussed in Sec. IV C is due to the strain and the distorted Si atom configuration at the interface.

The formation of peaks on the surface during the impact is discussed in Sec. IV D. Figure 16 shows two typical peak structures. Similar structures exist on the surface also before the impact, but some of them grow during the displacement phase, or new peaks appear. The origin of peaks is the local compression of the silica structure. The SiO_4 tetrahedra can move easily relative to each other; therefore, the tetrahedra can pile up at some locations during the displacement phase. Thus, the peaks are formed randomly in the displaced region. Larger displacements induce more peaks, which is seen in the simulations. Incomplete tetrahedra and Si–Si bonds can sometimes be found in peaks.

In a-Si, atoms are the basic building blocks and no larger rigid structures are available for peak formation. The simulated craters induced by 6 keV Ar_{43} impact on an a-Si target without the silica layer are very uniform and do not have outer rims or peaks around them (Fig. 17). The lateral forces are more uniform because there are not two elastically different layers present as in the a-SiO_2/c-Si system. Small lateral displacements similar to those found in silica were not observed in the simulations, because the a-Si does not have similar medium range order as found in silica. The results confirm that the effects of cluster impact in the surroundings of the impact point are different in a-Si and a-SiO_2, although in both cases the effect of the impact reaches over a wider area than the central crater and/or hillock area.

V. DISCUSSION

The diameters of central hillock areas can be considered to be the same in the simulations and in the experiments when the AFM tip convolution effect is taken into account. The central hillock is a typical crater form, which may include a narrow crater not seen with AFM, or the crater may have disappeared from the experimental samples during the oxidation process after the sample was moved from the UHV

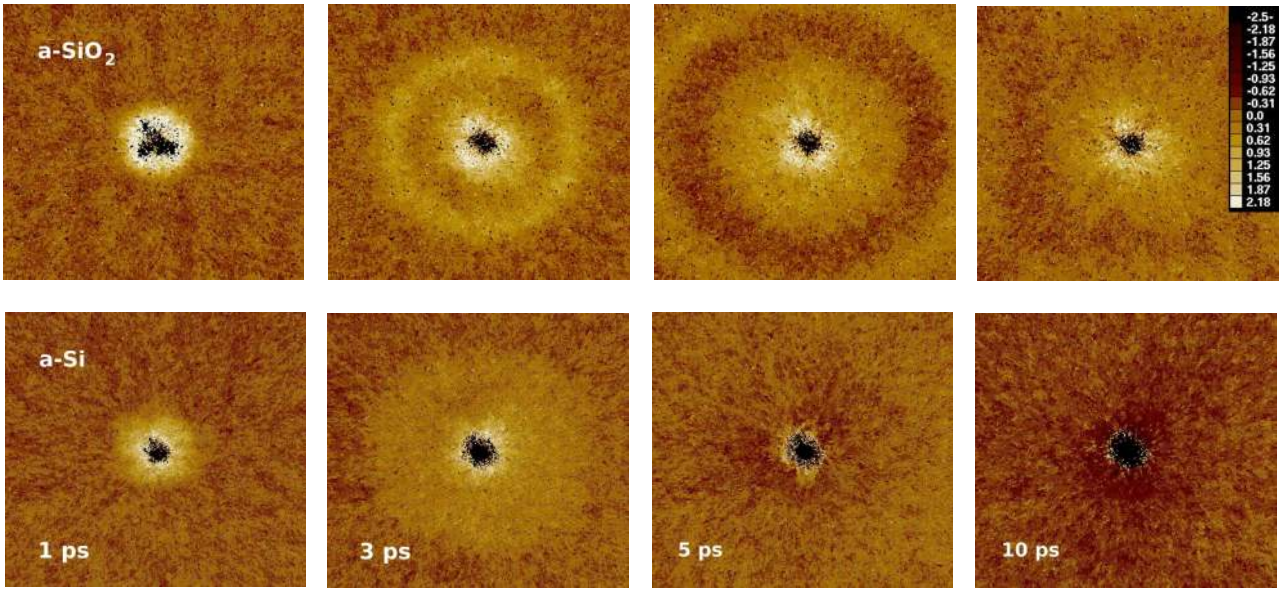

FIG. 11. (Color online) Visualizations of transient displacements induced by 60 keV Ar_{12} impacts on the a-SiO_2 substrate (upper row) and on the a-Si substrate (bottom row). Both substrates are without oxide layer. The colors show displacements relative to the origin as in Fig. 10. The snapshots from left to right are 1, 3, 5, and 10 ps after the impact. The size of the frames is 60×60 nm^2, which is the same as the size of frames in the upper row of Fig. 10.

conditions to the ambient atmosphere for the AFM measurement.

However, the heights of the hillocks are lower than in the experiments. The most probable reason for this is again the post-impact oxidation. Figure 10 shows that inside the crater, the silica layer is sputtered and a pure silicon surface is unmasked. Eventually, the oxidation process will produce a new silica layer in the bottom of the crater. Because this layer will develop also at the basement of the rims, it raises the rims up. In addition, the rims themselves contain extra silicon, which will react with the ambient oxygen and the volume of the rims may increase further. Allen *et al.* claim that the oxidation process forms a hillock over the crater and the height of the hillock could be 5 nm.[9]

In addition to differences between the experimental and simulated heights, there is another inconsistency between the experiments and simulations, which is not easy to explain by considering the properties of the potential and post-impact oxidation. The hillocks grow bigger with impact energy in the simulations, whereas the measured hillocks become lower with impact energy.[5] Usually, the size of the crater and rims begins to decrease when the clusters have enough energy to penetrate deeper inside the target, which happens at considerably higher energies than applied in the present simulations.[12,38,39] A possible explanation for the relatively deep penetration at these rather low energies is that the silica layer may contain voids or the density of the silicon substrate varies. At the moment, we are not able to confirm this. The effect of target preparation on the experimental results is discussed in Sec. IV A.

The AFM measurements show that a plateaulike structure around the central hillock exists more often in targets that support a native oxide layer than in targets without the layer. The high frequency of complex craters in oxide coated silicon can be indirectly related to the larger lateral momentum (Fig. 6) induced in the silica compared to the momentum induced in a-Si. Due to the larger lateral momentum, the displacements are stronger and changes in the surface layer are more probable in oxide than in a-Si (Figs. 10 and 11). However, the exact formation mechanism of the plateaulike regions (Fig. 4) is still unclear.

If we assume that the plateaus are of mechanical origin, and not the result of some electrical phenomenon that cannot be simulated with the classical molecular dynamics, the distribution of momentum during the impact and relaxation of the structure after impact is the most probable reason for their occurrence. According to the simulation, the displacement effect is clear when the cluster has enough energy to produce a cascade that reaches below the silica layer. Thus, the impact can affect the surface structure over a considerably larger area than the central crater area. If the structure contains voids or the density of the oxide layer is homogeneous, the changes may be larger. It is then possible that partial rims or plateaulike structures appear.

The differences between induced momentum distributions in different substrates indicate that topographical changes on the surface depend also on the thickness of the silica layer. If the lateral displacement of the silica and c-Si layers is the main reason behind the formation of the complex forms, the particular form that an impact produces depends on whether or not both layers are simultaneously affected. In other words, the effect is different if the displacement cascade reaches through the silica layer, which depends on the thickness of the layer and on the cluster energy. In addition, if the underlying layer is not a perfect c-Si structure, less energy is carried away by the elastic waves and the surface modifications may be stronger. A large number of simulations would be needed to verify the average surface modification probabilities for different thicknesses of silica layers and for different defect configurations in the underlying c-Si layer.

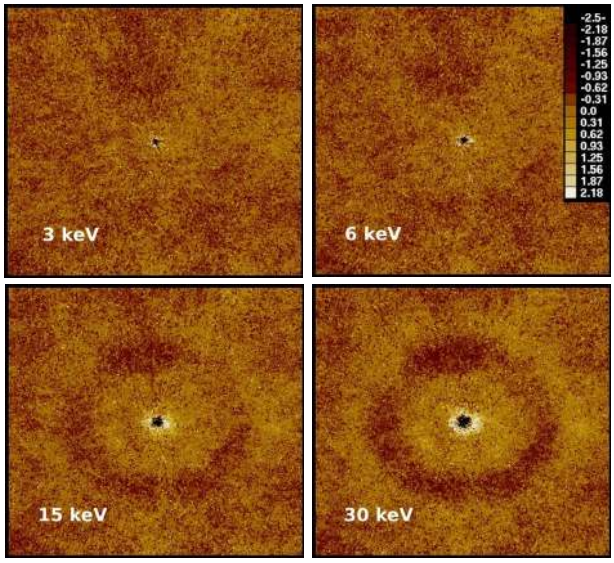

FIG. 12. (Color online) Displacements at 5 ps after Ar_{43} impacts on the a-SiO_2/c-Si target at different energies. The colors show displacements relative to the origin as in Fig. 10. The frames are 100×100 nm^2.

Such a comprehensive study is not possible at the moment.

Next, we exclude two other mechanisms, melting of the structure and conduction of energy by electrons, that induce structural changes but are not a possible reason for the formation of plateaulike structures in this case. The total destruction of the bonding in a homogeneous oxide layer is not an explanation for the 30–60 nm outer rims or plateaulike structures observed in the AFM measurements, because the cluster energies are not high enough to destroy areas as large as those enclosed by the outer rims. Here, the comparison of the cluster-surface energetic interaction with short-pulse laser irradiation is relevant. The threshold fluence for destruction of the native oxide layer by an ultrashort laser pulse is 0.256 keV/nm^2.[47] If we suppose that the energy of a cluster is uniformly deposited on the oxide surface, the diameter of the damaged area is 5.5 nm at 6 keV/cluster and 17.3 nm at 60 keV/cluster. The experimental outer rim diameter for the impact of 6 keV Ar_{12} cluster is 35 ± 5 nm.[5] In addition, a 60 keV cluster penetrates deeper in the target, only a portion of the energy will be released in the oxide layer, and the outer diameter of the simulated crater area is less than 10 nm (Fig. 10).

The second excluded mechanism for topographical changes is the energy diffusion by electrons from the impact region to the surroundings. This mechanism is studied in laser ablation experiments, where uniform plateaulike structures are also observed. There are several damage mechanisms with different threshold fluences that produce the complex laser ablation craters.[47–49] Among these mechanisms are the melting of the supporting c-Si layer and the diffusion of energy by conduction band electrons in silica.[49] However, these mechanisms affect the area of initial energy deposition, and the rims observed in laser ablation studies follow the fluence contours of the incident laser pulse.[48] Because the energies in cluster bombardment are considerably smaller and the energy is deposited in a very small region within the rim structure, it is not probable that these mechanisms would cause the outer rim, which is much larger that the initial energy deposition area. (The size of the affected region in laser ablation experiments is more than 10 μm wide, while the cluster impacts affect areas that have diameter typically less than 0.1 μm.)

In addition, there are two mechanisms which are not probable reasons for the plateaulike structures. Metal clusters fragment after they have sputtered and part of their atoms deposit back on the surface.[38,50,51] However, no large clusters were sputtered in the simulations and the crater is not large enough to provide the material needed to form plateau with diameters of 30–60 nm. During the displacement, some cracks may appear in the silica layer. Then, the ambient oxygen could react with unveiled silicon atoms in the silica layer and the layer becomes thicker. No cracks were observed in the simulations. (Cracks appear in quartz in impact simulations.)

The interatomic potentials used in the simulation always affect the results. Especially in impact simulations, some quantities are more sensitive to the choice of potential than others. For example, in c-Si, rim forms and heights depend on potential.[12] Therefore, it is possible that the details of the interatomic potential used in the calculations affect the peak formation and hillock height. The peaks and hillocks are consequences of changes in mutual positions of SiO_4 tetrahedra; thus, their height depends on how the angular dependence of Si–O–Si bonding is described in the potential. The potential used in this study describes the angular dependence in the same way as the well-tested Stillinger-Weber potential for Si (Appendix). However, the mathematical model is more complicated. In spite of this critical remark, we believe that the current silica potential describes the interactions quite well and no major artificial effects occur in the simulations.

In summary, the diameter of the effected area, where inelastic modifications are possible, is around 50 nm in the amorphous substrates simulated in this study. It is considerably more than the typical collision cascade or crater diameters. Permanent surface modifications are possible within this area, as we have shown. These modifications can be called long-range effects when compared to crater and hillock dimensions. Although the long-range effects are weak, they may effect how the smoothening of the surface or pattern formation on the surface occurs during cluster bombardment. They may also induce changes in density. For example, Brongersma *et al.*[52] have observed an overall densification and stress relaxation in silica films under MeV range Xe ion bombardment. This can be explained by a thermal spike model, where it is assumed that every impact melts a surface region, and the melted regions induce a macroscopic deformation when the substrate is a subject of irradiation for a sufficiently long time.[53,54] However, a typical cross section of a melted region is only 20 nm^2.[52] We have shown that even at lower impact energies, a cluster impact can induce changes over considerably larger surface regions. Whether or not these weak long-range effects induce permanent modifications on surfaces at medium or high cluster fluences is an open question.

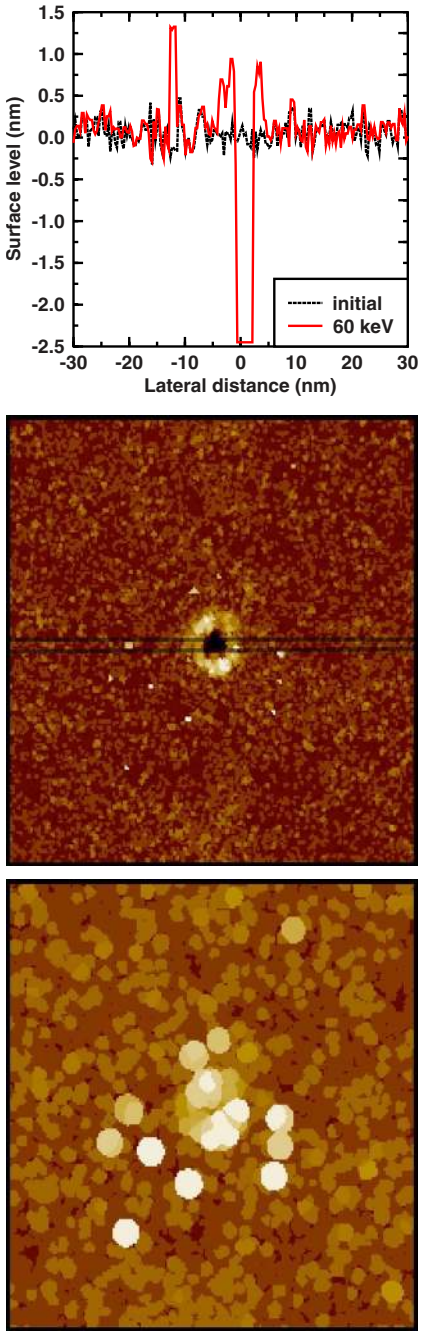

FIG. 13. (Color online) (a): Profile of the silica surface after a simulated impact of a 60 keV Ar_{12} cluster. Both the initial and the final surface levels are shown. (b): The top view of the same surface. The high areas are shown with lighter shade than the low areas. The surface profile shown in the upper frame represents the area between the horizontal lines. (c): The top view of the surface when analyzed with an "AFM tip" having a 2 nm radius of curvature. Due to the AFM tip convolution effect, the surface profile shown in the upper frame cannot be directly compared with this view.

VI. CONCLUSIONS

We have measured with AFM the complex crater structures induced in native oxide covered Si(111). The structures induced by cluster impact are different on the targets covered with a native oxide layer than on the pure silicon structures. In addition, the coexistence of complex (with hillocks) and simple craters on the same surface is verified in the AFM measurements.

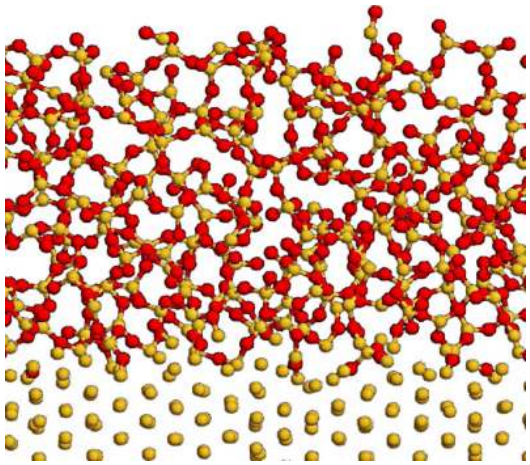

FIG. 14. (Color online) Silicon oxide layer before the impact. The average thickness of the layer is 2 nm. The Si and O atoms are represented by yellow and red spheres, respectively.

To study the crater formation, we simulated Ar cluster impacts on four substrates: *c*-Si lattice covered with 2 nm oxide layer, pure *a*-Si, pure *a*-SiO_2, and *c*-Si substrates. The results show differences in energy and momentum deposition, which indicate that the crater structures and probabilities of surface modification around the crater are different in these substrates. In particular, relatively large lateral momentum is induced in the silica layer, which is a possible reason for the complex crater forms observed experimentally, if the substrate is not homogeneous or contains voids.

However, the complex crater forms are not directly seen in the simulations. Contrary to the experiments, the simulations show that the craters produced on cluster impact are very uniform and they are almost the same size. The most probable explanation for these disagreements is that the homogeneous and pure substrate structures in the simulations are not completely comparable to the real substrates used in the experiments. We have also shown that some alternative explanations, such as destruction of bonds in the silica layer or energy diffusion by electrons, cannot explain complex crater forms.

On the other hand, simple hillocks that have the same diameter as the measured hillocks are observed in the simulations, which indicates that the formation of surface modifications is in some cases well reproduced by classical molecular dynamics. Moreover, our results show that rims of the simple craters with narrow openings can be imaged as hillocks due to the AFM tip convolution. The difference in height of the simulated and the experimentally measured hillocks is most probably caused by the oxidation of the damaged areas after the exposure of the samples to the ambient atmosphere prior to the AFM measurements. The growth of a thin oxide layer can increase the height of the surface features.

The results of this study demonstrate that the effects of cluster impact are quite complex in reality, and molecular

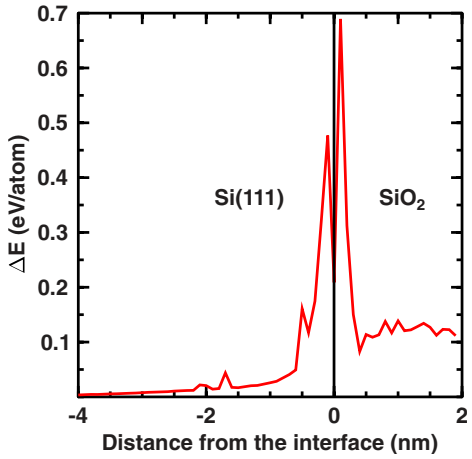

FIG. 15. (Color online) Average excessive strain energy of the atoms in the SiO_2/Si(111) interface before the impact. The zero level corresponds the energies in ideal bulk *c*-Si (below the interface) and SiO_2 structure (above the interface). The reference values for SiO_2 are based on Hartree-Fock calculations (Ref. 21).

dynamics simulations with ideal systems give only partial answers to the question of what are the mechanisms leading to surface modifications. The possible variations of the silica-silicon structures are numerous, and more experiments and simulations are needed to analyze energy deposition and cluster stopping in these structures in order to get a better understanding of the underlying dynamics.

ACKNOWLEDGMENTS

We thank T. Watanabe for helping us implement the potential. Generous grants of computer time from the Center for Scientific Computing in Espoo, Finland are gratefully acknowledged. This work was performed within the Finnish Centre of Excellence in Computational Molecular Science (CMS), financed by The Academy of Finland and the University of Helsinki. The authors from Gothenburg University acknowledge support of the Swedish Research Council (VR).

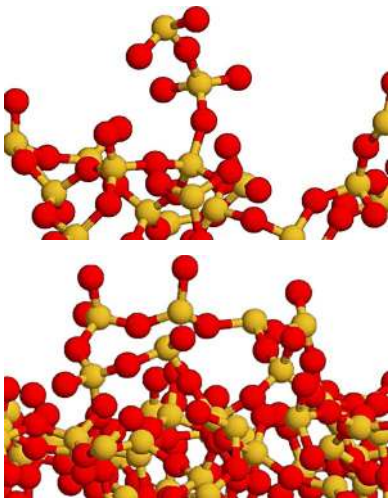

FIG. 16. (Color online) Two examples of peaks on the oxide surface after an impact of a 60 keV Ar_{12} cluster. The Si and O atoms are represented by yellow and red spheres, respectively.

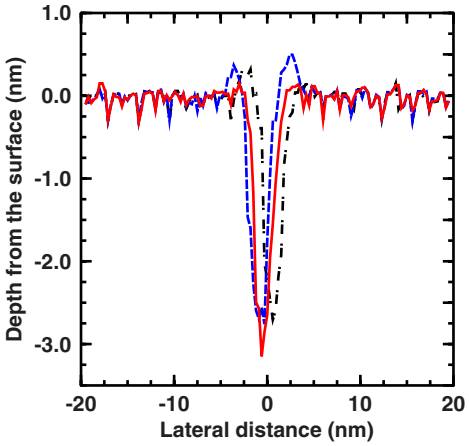

FIG. 17. (Color online) Surface profiles after three impacts of 6 keV Ar_{43} clusters on *a*-Si target.

APPENDIX: SILICA POTENTIAL

In the silica potential,[21] the total potential energy V of the simulated system is

$$V = \sum_i \sum_{j>i} \epsilon f_2(i,j) + \sum_i \sum_{j\neq i} \sum_{k>jk\neq i} \epsilon f_3(i,j,k), \quad \text{(A1)}$$

where ϵ is the energy unit (50 kcal/mol) introduced by Stillinger and Weber. The two-body term is

$$f_2(i,j) = g_{ij} A_{ij} (B_{ij} r_{ij}^{-p_{ij}} - r_{ij}^{-q_{ij}}) \exp[(r_{ij} - a_{ij})^{-1}]. \quad \text{(A2)}$$

The length unit is the same as in the Stillinger-Weber potential $\sigma = 2.0951$ Å. The three-body term is

$$f_3(i,j,k) = \Lambda_1(i,j,k)\Theta_1(\theta_{jik}) + \Lambda_2(i,j,k)\Theta_2(\theta_{jik}), \quad \text{(A3)}$$

$$\Lambda_n(i,j,k) = \lambda_{n,jik} \exp\left[\frac{\gamma_{n,jik}^{ij}}{r_{ij} - a_{n,jik}^{ij}} + \frac{\gamma_{n,jik}^{jj}}{r_{ij} - a_{n,jik}^{ik}}\right], \quad \text{(A4)}$$

$$\Theta_n(i,j,k) = (\cos\theta_{jik} - \cos\theta_{n,jik}^0)^2 + \alpha_{n,jik}(\cos\theta_{jik} - \cos\theta_{n,jik}^0)^3, \quad \text{(A5)}$$

$$\lambda_{n,jik} = \mu_{n,jik}\{1 + \nu_{n,jik} \exp[-\xi_{n,jik}(z - z_{n,jik}^0)^2]\}. \quad \text{(A6)}$$

The *bond softening function* $g(i,j)$ controls the two-body term in the silica potential according to the coordination numbers of atoms i and j. The following function is effective only for Si-O pairs:

$$g_{ij} = \begin{cases} g_{\mathrm{Si}}(z_i) g_{\mathrm{O}}(z_j), & i = \mathrm{Si} \text{ and } j = \mathrm{O} \\ g_{\mathrm{Si}}(z_j) g_{\mathrm{O}}(z_i), & i = \mathrm{O} \text{ and } j = \mathrm{Si} \\ 1 & \text{otherwise}, \end{cases} \quad \text{(A7)}$$

$$g_{\mathrm{Si}} = \begin{cases} p_4 + (p_1\sqrt{z+p_2} - p_4)\exp([p_3/(z-4)]\ , & z < 4 \\ p_4, & z \geqslant 4, \end{cases} \tag{A8}$$

$$g_{\mathrm{O}}(z) = \frac{p_5}{\exp[(p_6 - z)/p_7] + 1} \exp[p_8(z - p_9)]^2, \tag{A9}$$

where z_i is the coordination number of the ith atom to heterotype atoms:

$$z_i = \sum_{j \neq i} f_c(r_{ij}), \tag{A10}$$

$$f_c(r) = \begin{cases} 1, & r < R - D \\ 1 - \dfrac{r - R + D}{2D} + \dfrac{\sin[\pi(r - R + D)/D]}{2\pi}, & R - D \leqslant R + D \\ 0, & r \geqslant R + D. \end{cases} \tag{A11}$$

The parameters are given in Ref. 21.

In the present implementation, the bond softening is simplified so that $g_{\mathrm{Si}} = 1$ to achieve numerical stability. In addition, Eq. (A6) is different than published in Ref. 21.[55]

*juha.samela@helsinki.fi

[1] V. N. Popok and E. E. B. Campbell, Rev. Adv. Mater. Sci. **11**, 19 (2006).
[2] S. Tian, J. Appl. Phys. **93**, 5893 (2003).
[3] V. Popok, S. Prasalovich, and E. Campbell, Vacuum **76**, 265 (2004).
[4] V. Popok, S. Prasalovich, and E. Campbell, Nucl. Instrum. Methods Phys. Res. B **207**, 145 (2003).
[5] S. Prasalovich, V. Popok, P. Persson, and E. Campbell, Eur. Phys. J. D **36**, 79 (2005).
[6] H. Park, H.-J. Jung, K. Jeong, and W. Choi, Thin Solid Films **475**, 36 (2005).
[7] R. P. Webb, M. Kerford, M. Kappes, and G. Brauchlw, Nucl. Instrum. Methods Phys. Res. B **122**, 318 (1997).
[8] Z. Insepov, L. Allen, C. Santeufemio, K. Jones, and I. Yamada, Nucl. Instrum. Methods Phys. Res. B **202**, 261 (2003).
[9] L. P. Allen, Z. Insepov, D. B. Brenner, C. Santeufemio, W. Brooks, K. S. Jones, and I. Yamada, J. Appl. Phys. **92**, 3671 (2002).
[10] Y. Nakayama, S. Houzumi, N. Toyoda, K. Mochji, T. Mitamura, and I. Yamada, Nucl. Instrum. Methods Phys. Res. B **241**, 618 (2005).
[11] S. Ihara, S. Itoh, and J. Kitakami, Phys. Rev. B **58**, 10736 (1998).
[12] J. Samela, K. Nordlund, J. Keinonen, and V. Popok, Nucl. Instrum. Methods Phys. Res. B **255**, 253 (2007).
[13] I. Yamada, Eur. Phys. J. D **9**, 55 (1999).
[14] F. H. Stillinger and T. A. Weber, Phys. Rev. B **31**, 5262 (1985).
[15] F. H. Stillinger and T. A. Weber, Phys. Rev. B **33**, 1451 (1986).
[16] V. N. Popok, S. V. Prasalovich, M. Samuelsson, and E. E. B. Campbell, Rev. Sci. Instrum. **73**, 4283 (2002).
[17] G. Kornich, G. Betz, V. Zaporojtchenko, and K. Pugina, Nucl. Instrum. Methods Phys. Res. B **255**, 233 (2007).
[18] J. Samela, J. Kotakoski, K. Nordlund, and J. Keinonen, Nucl. Instrum. Methods Phys. Res. B **239**, 331 (2005).
[19] M. Ghaly, K. Nordlund, and R. S. Averback, Philos. Mag. A **79**, 795 (1999).
[20] K. Nordlund, M. Ghaly, R. S. Averback, M. Caturla, T. Diaz de la Rubia, and J. Tarus, Phys. Rev. B **57**, 7556 (1998).
[21] T. Watanabe, D. Yamasaki, K. Tatsumura, and I. Ohdomari, Appl. Surf. Sci. **234**, 207 (2004).
[22] K. Nordlund, N. Runeberg, and D. Sundholm, Nucl. Instrum. Methods Phys. Res. B **132**, 45 (1997).
[23] K. Nordlund, Comput. Mater. Sci. **3**, 448 (1995).
[24] J. F. Ziegler, J. P. Biersack, and U. Littmark, *The Stopping and Range of Ions Matter* (Pergamon, New York, 1985).
[25] F. Wooten, K. Winer, and D. Weaire, Phys. Rev. Lett. **54**, 1392 (1985).
[26] S. von Alfthan, A. Kuronen, and K. Kaski, Phys. Rev. B **68**, 073203 (2003).
[27] P. N. Keating, Phys. Rev. **145**, 637 (1966).
[28] T. Nakayama, Rep. Prog. Phys. **65**, 1195 (2002).
[29] T. Watanabea, K. Tatsumuraa, and I. Ohdomari, Appl. Surf. Sci. **237**, 125 (2004).
[30] K. Tatsumura, T. Watanabe, D. Yamasaki, T. Shimura, M. Umeno, and I. Ohdomari, Phys. Rev. B **69**, 085212 (2004).
[31] D. B. Asay and S. H. Kim, J. Chem. Phys. **124**, 174712 (2006).
[32] A. Munkholm and S. Brennan, Phys. Rev. Lett. **93**, 036106 (2004).
[33] S. Susman, K. J. Volin, D. L. Price, M. Grimsditch, J. P. Rino, R. K. Kalia, P. Vashishta, G. Gwanmesia, Y. Wang, and R. C. Liebermann, Phys. Rev. B **43**, 1194 (1991).
[34] X. Yuan and A. N. Cormack, J. Non-Cryst. Solids **319**, 31 (2003).
[35] S. Susman, K. J. Volin, D. G. Montague, and D. L. Price, Phys. Rev. B **43**, 11076 (1991).
[36] K. Nordlund, J. Keinonen, E. Rauhala, and T. Ahlgren, Phys. Rev. B **52**, 15170 (1995).
[37] I. P. Kozlov, V. B. Odzhaev, V. N. Popok, and V. Hnatowicz, Semicond. Sci. Technol. **11**, 722 (1996).
[38] J. Samela and K. Nordlund, Nucl. Instrum. Methods Phys. Res. B **263**, 375 (2007).
[39] J. Samela and K. Nordlund, Phys. Rev. B **76**, 125434 (2007).
[40] J. Samela, K. Nordlund, J. Keinonen, V. N. Popok, and E. E. B. Campbell, Eur. Phys. J. D **43**, 181 (2007).
[41] J. Samela and K. Nordlund (unpublished).
[42] P. Sigmund, J. Phys. (Paris) **50**, 175 (1989).
[43] C. Anders and H. M. Urbassek, Nucl. Instrum. Methods Phys. Res. B **258**, 497 (2007).
[44] L. Seminara, P. Convers, R. Monot, and W. Harbich, Eur. Phys. J. D **29**, 49 (2004).
[45] Y. Tu and J. Tersoff, Phys. Rev. Lett. **84**, 4393 (2000).
[46] J. D. Torre, J.-L. Bocquet, Y. Limoge, J.-P. Crocombette, E. Adam, G. Martin, T. Baron, P. Rivallin, and P. Mur, J. Appl. Phys. **92**, 1084 (2002).
[47] J. Bonse, K.-W. Brzezinka, and A. J. Meixner, Appl. Surf. Sci.

221, 215 (2004).
[48] J. P. McDonald, A. A. M. Y. N. Picard, and S. M. Yalisove, Appl. Phys. Lett. **86**, 264103 (2005).
[49] T. Q. Jia, Z. Z. Xu, R. X. Li, D. H. Feng, X. X. Li, H. Y. S. C. F. Cheng, N. S. Xu, and H. Z. Wang, J. Appl. Phys. **95**, 5166 (2004).
[50] A. Wucher, M. Wahl, and H. Oechsner, Nucl. Instrum. Methods Phys. Res. B **83**, 73 (1993).
[51] T. J. Colla, H. M. Urbassek, A. Wucher, C. Staudt, R. Heinrich, B. J. Garrison, C. Dandachi, and G. Betz, Nucl. Instrum. Methods Phys. Res. B **143**, 284 (1998).
[52] M. L. Brongersma, E. Snoeks, T. van Dillen, and A. Polman, J. Appl. Phys. **88**, 59 (2000).
[53] H. Trinkaus and A. I. Ryazanov, Phys. Rev. Lett. **74**, 5072 (1995).
[54] T. van Dillen, A. Polman, P. R. Onck, and E. van der Giessen, Phys. Rev. B **71**, 024103 (2005).
[55] T. Watanbe (private communication).